Journal of Materials Research and Technology 32 (2024) 1809–1819

Contents lists available at ScienceDirect

Journal of Materials Research and Technology

journal homepage: www.elsevier.com/locate/jmrt

Enhanced tribological properties and the microstructure evolution of the gradient nanostructured copper alloy

Rongjian Shi [a,b], Kaixuan Chen [a], Hui Fu [c], Kewei Gao [a], Xu-Sheng Yang [c,**], Xiaolu Pang [a,b,*]

[a] Beijing Advanced Innovation Center for Materials Genome Engineering, School of Materials Science and Engineering, University of Science and Technology Beijing, Beijing, 100083, China
[b] State Key Laboratory of Nuclear Power Safety Technology and Equipment, University of Science and Technology Beijing, Beijing, 100083, China
[c] State Key Laboratory of Ultra-precision Machining Technology, Department of Industrial and Systems Engineering, The Hong Kong Polytechnic University, Hung Hom, Kowloon, Hong Kong, China

ARTICLE INFO

Keywords:
Copper alloy
Tribological property
Friction and wear
Gradient microstructure
HRTEM

ABSTRACT

In this work, the effects of the gradient microstructures by surface mechanical attrition treatment (SMAT) on the corresponding tribological properties of the nanoprecipitates strengthened copper alloy was investigated. The nanoprecipitates strengthened copper alloy possesses a decent tribological properties compared with the pure copper and bronze. The SMAT-processed NP&T alloy possesses distinctly lower coefficients of friction (COF) than its coarse-grained counterpart throughout the entire frictions. In particular, under a sliding load of 2 N, NP&T alloy possesses a lower COF of 0.58 ± 0.03, approximately 15% lower than that of its homogeneous counterpart. Additionally, the wear volumes, wear rates, and worn surface roughness were approximately 45% lower in the NP&T alloy, indicating the superior tribological properties. The macro-, micro-, and atomic-scale friction and wear mechanisms in the worn NP&T alloy were systematically determined. The inherent gradient nanostructures could achieve strain delocalization, thereby suppressing surface deformation and improving wear resistance. Wear-induced substructure in the NP&T alloy comprises gradient layers mediated by twinning and stacking faults combined with nanocomposite layers, resulting in novel tribological performance characteristics. Thus, combining inherent and newly formed wear-resistant gradient nanostructures is an effective design strategy for high-performance Cu alloys.

1. Introduction

Enhancing performance through microstructural optimization, such as controlling structural defects like dislocations and boundaries, is a primary goal of materials science research [1–5]. Copper alloys have been widely used for millennia, primarily because of their excellent mechanical performance [6]. These alloys are used in various industrial applications, including sleeve bearings and wheel gears [7–10]. Although the tribological performance is one of the most significant properties for these copper alloys, the presence of numerous microstructures can counterintuitively impair their resistance to friction and wear. Therefore, there is an urgent need to further design and improve next-generation wear-resistant Cu alloys with novel tribological performance by controlling these imperfections.

The Archard equation [11,12] empirically demonstrates that ultra-high hardness enhances the resistance to friction and wear. Uniformly homogeneous nanograined (NG) materials normally have extremely high hardness through the Hall–Petch relation [13,14]. However, the coefficient of friction (COF) and wear rates of NG metals and alloys are often lower than those of coarse-grained (CG) components, especially under conditions of high sliding speeds or loads [15,16]. For instance, surface roughening and delaminating are observed in NG metals with relative high COF. This is mainly due to the highly limited dislocations multiplication and plastic deformation capacity of NG materials, which result in delaminating tribolayers and poor tribological performance [17]. Recently, the heterogeneous gradient NG (GNG) surface layer in Cu alloys has been shown to considerably reduce the COF and wear rate compared with homogeneous NG and CG alloys

* Corresponding author. Beijing Advanced Innovation Center for Materials Genome Engineering, School of Materials Science and Engineering, University of Science and Technology Beijing, Beijing, 100083, China.
** Corresponding author.
E-mail addresses: xsyang@polyu.edu.hk (X.-S. Yang), pangxl@mater.ustb.edu.cn (Xiaolu Pang).

https://doi.org/10.1016/j.jmrt.2024.08.036
Received 28 May 2024; Received in revised form 16 July 2024; Accepted 7 August 2024
Available online 8 August 2024

[18]. This improvement can be mainly attributed to the ability of GNG substructures to accommodate severe plastic deformation and suppress sliding-induced strain localization [15,17].

Gradient nanostructured (GNS) metals have been widely engineered to overcome their strength–ductility trade-off dilemma and increase the strain hardening [19,20]. Various fabrication approaches [2,21,22], such as surface mechanical attrition treatment (SMAT) [5,23], surface mechanical grinding treatment [1,17,24–27], and ultra-precision machining technologies [28–30], have been developed to effectively synthesize gradient nanoscale microstructures with superior mechanical performance and outstanding friction and wear resistance.

However, a comprehensive understanding of the mechanisms of microstructural evolution and the influence of the near-surface worn substructures at macroscopic and atomic scales is still lacking. The in-situ formation of gradient amorphous-crystalline nanocomposite layer is presented to intensively improve the superior wear resistance [31–33]. For instance, an in-situ submicrometer-thick $Ti_{17}Nb_{13}Zr_{13}$-Fe_2O_{55} layer combined with a nanoscale Ag nanocomposite substantially reduced the wear rate in TiNbZr–Ag alloy through reactive wear protection [32]. This nanocomposite exhibited a high strength and superior homogeneous plastic flow behavior to improve the wear resistance. Furthermore, the strategy of self-adaptive gradient nanostructures during the sliding of TaMoNb film was proposed to achieve superior wear resistance in our previous work [31]. The amorphous matrix-nanograins composite layer and the underneath gradient layer accelerate the coordinated plastic deformation and restrain the wear-induced localized cracking. For the Cu–tungsten carbide (WC) tribo-system sliding in ambient air, the fundamental oxidation process is the nucleation of oxygen-enriched Cu nanoparticles; the resulting Cu_2O oxide forms mixed tribolayers [34]. These observations motivate further investigation into the effects of near-surface worn substructures on the tribological performance and underlying wear mechanisms in Cu alloys.

This present study systematically investigates the enhanced tribological performance of the GNS Cu alloys. The SMAT technique was performed to fabricate a gradient Cu alloy. Microstructural characterization was conducted before and after SMAT using transmission electron microscopy (TEM), the scanning TEM (STEM)-energy-dispersive X-ray spectroscopy (EDS), and high-resolution TEM (HRTEM) observations. Tribological properties such as COFs, wear volumes, wear rates, and worn surface roughness were thoroughly analyzed. The underlying mechanisms of microstructural evolution and the influence of the gradient structure were systematically studied through macro-, micro-, and atomic-scale observations. This study aims to guide the design of gradient self-organized wear-induced layers to achieve wear-resistant Cu alloys.

2. Experimental procedure

2.1. Materials

The Cu alloy considered in this study is a type of tin–bronze alloy with the composition Cu–12Sn-1.5Ni-0.6Fe (wt.%). The fabrication methods and processes are described elsewhere [5,10]. Annealed nanoprecipitate-strengthened alloy (denoted “NP”) with the thickness of 1.2 mm was subjected to SMAT at a 20 kHz vibration frequency using 3-mm bearing balls for 5 min. SMAT process was performed on a single surface of the NP samples at room temperature. The SMAT processed alloy is denoted “NP&T”.

2.2. Microstructural characterization

The samples before and after SMAT were mechanically polished and then electropolished. The original and SMAT-processed microstructures were observed by electron backscatter diffraction (EBSD, JSM-7900F operated at 20 kV) with the step size of 0.04 μm for micro-observations. The microstructure, grain size distribution, and EDS spectra of the alloys before and after applying friction were examined using TEM (JEOL JEM-2100F) operated at 200 kV. Plane view TEM and HRTEM were also conducted on foil specimens at specific depth layers to investigate the wear mechanisms.

2.3. Friction and wear testing

Before performing the friction tests, samples were polished mechanically and progressively, then polished with a silica polishing agent. All samples were finally float polished to achieve equivalent surface roughness (R_a ~0.002 μm and R_z ~ 0.010 μm). Dry sliding tests were performed on the NP and NP&T specimens using a ball-on-plate contact configuration (CETR UMT2 oscillating friction tester) at ambient temperature in air. WC-Co balls with a diameter of 10 mm and a microhardness of 91 HRA were used. Friction and wear tests were performed with a 15 mm sliding stroke, a 60 rev/min (0.03 m/s) sliding velocity, and normal loads of 2, 5, and 10 N. The COF, μ, is defined as: $\mu = F/P$, where F and P are the frictional force and the applied normal load, respectively. The COF values were determined automatically using the UMT Viewer software.

2.4. Worn surface and intersectional observation

Worn surfaces were observed using a confocal laser scanning microscope (CLSM, LEXTOLS4000) to determine the wear volumes, V_w, under different sliding conditions. A reference surface was used to quantify the volume of a wear track, and the volume loss of the material underneath the reference surface was taken as the wear volume. $V_w = SL$, where S is the worn area and L (15 mm) is the oscillating stroke. The worn area could be obtained from the CLSM system. At least 10 profiles for each sample under each condition were taken to calculate the representative worn area for each wear volume value. The worn area both below and above the initial surface (e.g., the abrasive debris) was integrated on each cross-section [12]. The corresponding wear rates were then obtained as wear volume per unit load and per unit distance after applying friction. The variation of surface roughness was measured by CLSM. The worn surface morphologies were characterized by SEM. For the worn NP&T subsurface, cross-sectional TEM specimens were fabricated at the middle of the worn track using the focused ion beam (FIB) milling technique. The standard lift out process was executed on a Thermo Scientific Helios G4 CX FIB–SEM workstation. A Pt layer was deposited on the worn surface before the FIB milling to protect the worn substructure from beam damage. Finally, thin FIB films were observed by TEM, EDS, and HRTEM to explore the wear mechanisms.

3. Results and discussion

3.1. Microstructural observation before friction and wear

The microstructures of the NP and NP&T alloys before friction and wear are shown in Fig. 1. Typical cross-sectional EBSD micrographs of NP and NP&T alloys are depicted in Fig. 1(a)–(c) and (d)–(f), respectively. Fig. 1(a–d) and (b, e) are the EBSD image quality and inverse pole figure maps, respectively. Fig. 1(c) depicts the phase map decorated with the grain boundaries (marked by “GB”) of the NP alloy, indicating single phase fcc Cu. The NP sample contains random coarse grains with dozens of micrometers. Fig. 1(f) is the kernel average misorientation map corresponding to Fig. 1(d–e) in the NP&T sample, reflecting the geometrically necessary dislocation densities. After SMAT, the NP&T sample displays a ~20-μm-thick typical gradient microstructure, included a grain distributionand dislocation density.

Before conducting the friction and wear tests, the topmost surface of the NP&T specimen was subtly characterized by TEM technique, as indicated in Fig. 2. The overall bright field TEM micrograph is presented in Fig. 2(a), indicating the distribution of the substructures. Ultra-fined grains (UFGs) are clearly observed with the dispersed nanoscale

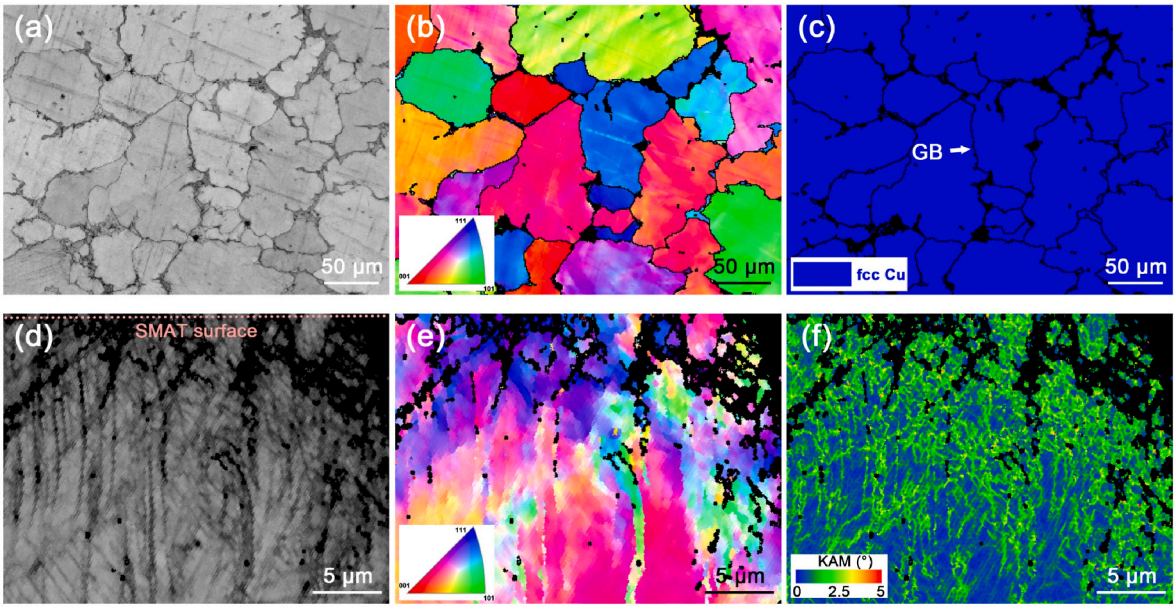

Fig. 1. EBSD characterization of the studied (a–c) NP alloy and (d–f) SMAT-processed NP&T alloy. (a, d) The EBSD image quality maps; (b, e) the EBSD inverse pole figure images; (c) the phase map of NP alloy, showing the single-phase fcc Cu; (f) kernel average misorientation map of the NP&T alloy.

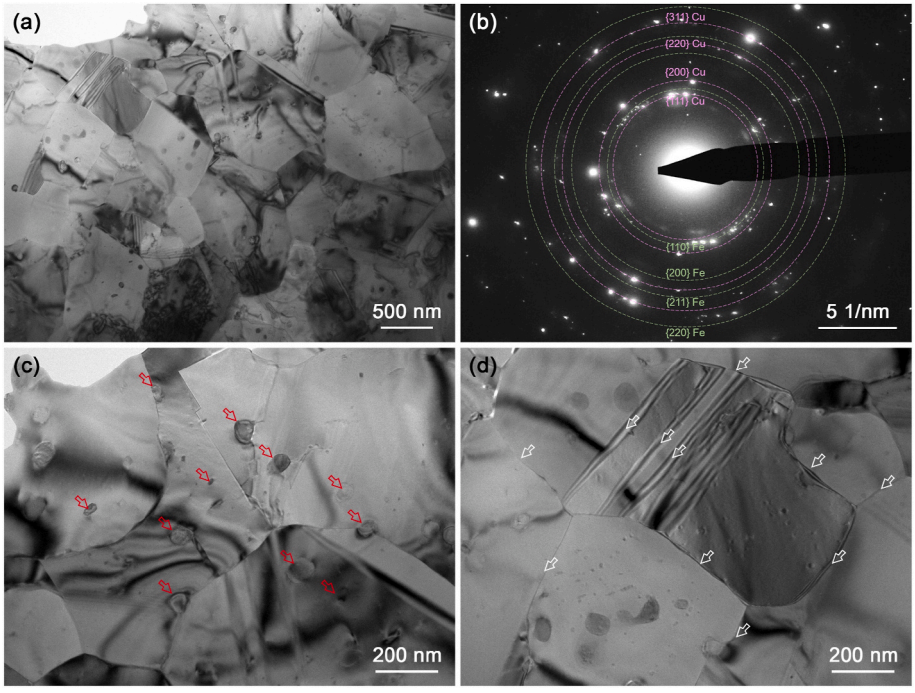

Fig. 2. Microstructural TEM characterization of the investigated NP&T alloy. (a) The overall TEM bright-field image, indicating the distribution of the substructures. (b) The corresponding SAED pattern of the selected region in (a). (c) Enlarged TEM bright-field image of the distribution of precipitates marked by the red arrows. (d) Magnified view of the grain boundaries marked by the white arrows.

precipitates. The selected area electron diffraction (SAED) pattern of the selected area in Fig. 2(a) is indicated in Fig. 2(b). The measured lattice spacings of the SAED pattern is listed in Table 1. Two types of diffraction spots were detected, corresponding to the fcc Cu and bcc Fe phases, as indicated by the violet and green rings, respectively. The enlarged subtle TEM images in Fig. 2(c) and (d) indicate high-density nanoprecipitates (red arrows) and grain boundaries (white arrows), respectively. To further investigate the distribution of the alloy elements, details of the subtle composition of the topmost surface of the SMAT-processed microstructure in NP&T alloy are indicated in Fig. 3. Fig. 3(a) is the high-angle annular dark field (HAADF) micrograph of the precipitates and twins inside the UFGs. The EDS mapping of Cu, Ni, Fe, and Sn are displayed in Fig. 3(b–e), respectively, showing that nanoscale Fe-enriched precipitates are dispersed within the grains with uniformly distributed elements. The precipitates-strengthened and SMAT-processed microstructures were systematically investigated in previous studies [5]. These abundant grain boundaries and precipitates dispersed in the UFGs are certain to influence the tribological properties of the SMAT-processed NP&T alloy, as examined in the following section.

Table 1
The measured lattice spacings of the SAED pattern in Fig. 2(b).

Lattice spacing (SAED), Å	Lattice planes	Lattice spacings (Calc), Å
2.118	{111} fcc-Cu	2.09 A
2.016	{110} bcc-Fe	2.02 A
1.825	{200} fcc-Cu	1.81 A
1.387	{200} bcc-Fe	1.43 A
1.280	{220} fcc-Cu	1.28 A
1.205	{211} bcc-Fe	1.17 A
1.093	{311} fcc-Cu	1.09 A
0.986	{220} bcc-Fe	1.01 A

3.2. Tribological properties

3.2.1. COFs and surface morphologies

Bronze alloys are extensively used in tribological applications, e.g., bushings, gear, and bearings in mining and manufacturing equipment, highlighting the importance of tuning microstructures to enhance the tribological performance [7,9,35]. In this section, we performed the friction and wear tests to evaluate the tribological properties of precipitates–strengthening bronze alloy before and after SMAT, as show in Fig. 4. The measured COFs tend to a steady state rapidly after 300 s for both NP and NP&T specimens under normal loads of 2, 5, and 10 N, as depicted in Fig. 4(a1–a3). Additionally, 3D CLSM illustrating surface morphologies of the NP and NP&T samples under various loads are displayed in Fig. 4(b–e). As the sliding load increased, cracks, scars, and pileups of microscale heights and depths became more pronounced in the NP sample, indicated by arrows in Fig. 4(c) and (e). In contrast, the NP&T exhibited more alleviative surface features, aliging with the trend observed in COFs. Representative 3D CLSM side views of surface morphologies in Fig. 4(b–e) were also analyzed to quantify wear volumes and wear rates.

The variations in the steady-state COFs as a function of sliding loads are summarized in Fig. 5(a and b), showing that COFs gradually decreased with increasing the sliding loads. The nanoprecipitates strengthened copper alloy possesses a decent COF (e.g., 0.58 at 10 N), compared with the traditional CG Cu and bronze. Furthermore, it is interesting to reveal that the SMAT-processed NP&T possessed distinctly lower COFs than NP sample throughout the entire frictions, e.g., 0.69 ± 0.03 for NP and 0.58 ± 0.03 for NP&T (reduced by ~15%) under a sliding load of 2 N (Fig. 5(a)). Besides, the COFs of NP&T are also lower than those of similar Cu alloy [36], CG Cu, and SMAT Cu in previous studies (Fig. 5(b)) [17,37]. Furthermore, quantitative analyses were conducted on the wear volumes, wear rates, and worn surface roughness (R_a and R_z) to elaborate on the tribological properties, as summarized in Fig. 5(c–f). These results will be discussed in detail in the following sections.

3.2.2. Wear volumes and wear rates

The wear depth was shallower for the NP&T sample than the NP sample across all loading conditions. To quantitatively assess the wear resistance, the area both below and above the initial surface were integrated to calculate the wear volumes and wear rates [12], as summarized in Fig. 5(c and d), respectively. Three tests were performed per condition in three or more different locations. It should be noted that the plastic deformation and the wear loss of the WC-Co balls are trivial [34]. The COFs are decreased with increasing the sliding load, while the wear volumes are increased on the contrary. Besides, those samples with lower COFs usually possess lower wear volumes and wear rates. Wear volumes continued to accumulate with increasing sliding load, with the NP&T sample consistently exhibiting considerably reduced wear volumes and better load bearing capacity compared to the NP. For instance, under a sliding load of 10 N, wear volumes were $(4.68 \pm 0.67) \times 10^6$ μm^3 for NP and $(3.31 \pm 0.54) \times 10^6$ μm^3 for NP&T. Meanwhile, the obtained wear rates for the NP&T specimen are much smaller than those for NP counterpart under different sliding loads. The wear rate reached the maximum peak under the sliding load of 5 N for both alloys (Fig. 5 (d)). This is mostly ascribed to the competition between the formation rate of the newly formed wear-resistant structures and the surface abrasion rate, which still needs further investigations in the future.

3.2.3. Worn surface roughness

Variations in the measured surface roughness perpendicular to the sliding direction under all conditions were also evaluated. The roughness R_a and R_z are summarized in Fig. 5(e) and (f), respectively. As the sliding load increased, the worn surface roughness progressively increased. The NP sample exhibited deeper scars and more severe sliding-induced surface roughening, even under moderate loads, such as 2 N. However, the NP&T surface presents higher roughening resistance, which is different from the NP sample, especially for the sliding loads of 2 N and 5 N. The tendency is consistent with the COFs, wear volumes, and wear rates for the NP and NP&T alloys, indicating the superior tribological properties in NP&T alloy. The friction and wear mechanisms in NP&T alloy will be revealed in the next part.

3.3. Friction and wear mechanisms

3.3.1. Macro-scale observation

Respective SEM micrographs of worn surfaces are shown in Fig. 6, illustrating that the NP sample exhibited denser and larger delamination

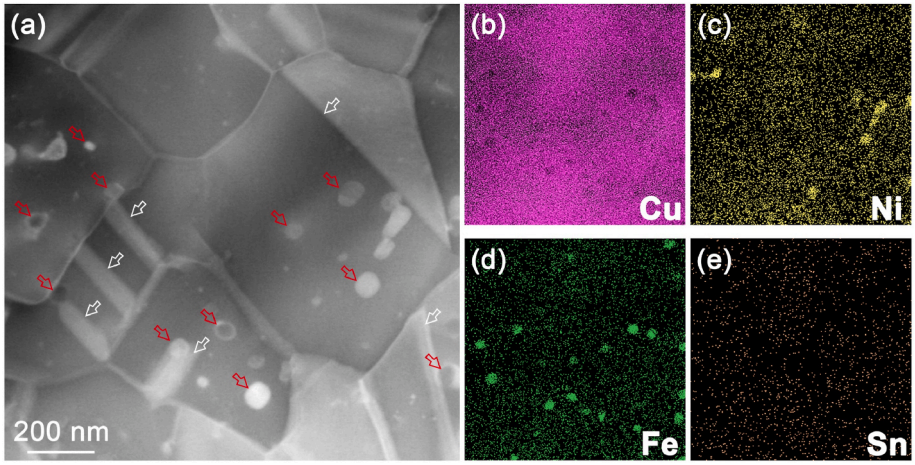

Fig. 3. The STEM-EDS mapping of the topmost surface of the SMAT-processed microstructure in NP&T alloy: (a) the HAADF image, EDS mapping of the region in (a) showing the chemical compositions of (b) Cu, (c) Ni, (d) Fe, and (e) Sn.

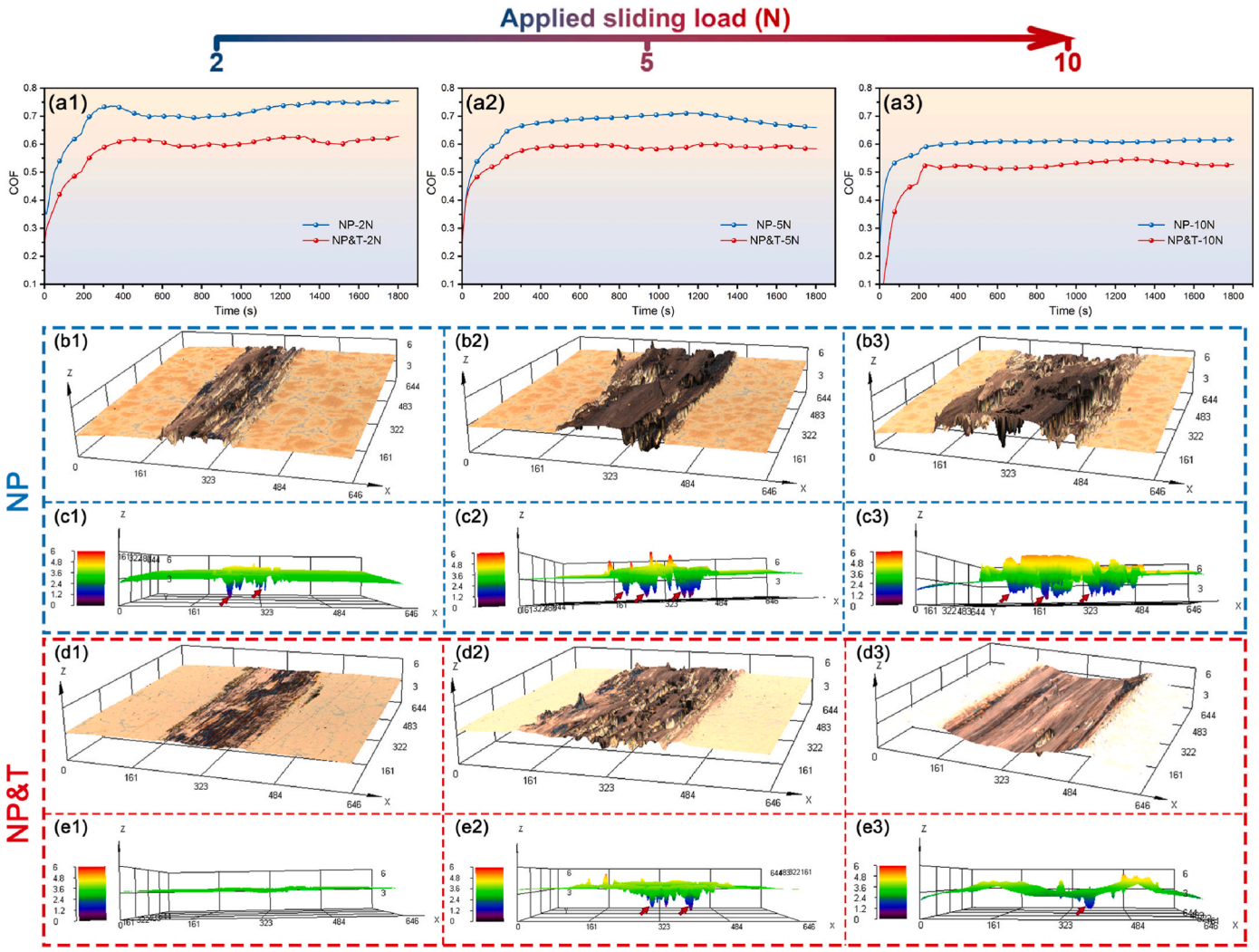

Fig. 4. Variations of COFs and surface morphologies of NP and NP&T specimens sliding against WC–Co balls under loads of 2 N, 5 N, and 10 N in 30 min (1800 s). COFs versus sliding time under loads of (a1) 2 N, (a2) 5 N, and (a3) 10 N. 3D CLSM profiles for the worn subsurface structure to measure the wear volumes and wear rates of (b–c) NP and (d–e) NP&T samples under loads of (b1, c1, d1, e1) 2 N, (b2, c2, d2, e2) 5 N, and (b3, c3, d3, e3) 10 N.

cracks and pileups compared to the NP&T sample under each load condition. The occurrence of worn cracks (marked by the arrows) increased with higher sliding loads, particularly noticeable in the NP alloy. Nevertheless, the worn surfaces of the NP&T in Fig. 6(d–f) indicate mild abrasion and less cracks. Inset in Fig. 6(f) shows the detail of the smooth plastic zone in NP&T sample under sliding load of 10 N. The micro- and atomic-scale observations through FIB and TEM characterizations will be conducted to further uncover the underlying wear-resistant mechanism in NP&T alloy.

3.3.2. *Micro-scale observation*

FIB milling was conducted at the worn surface of the NP&T alloy after applying friction for 1800 s under the sliding load of 10 N. Cross-sectional SEM and TEM characterizations are indicated in Fig. 7. The dashed line in Fig. 7(a) identifies the worn boundary on the SEM micrograph of the worn subsurface. The lift-out FIB technique was conducted at the rectangle area with a sliding-induced crack in Fig. 7(b), enlarged from the dotted region in Fig. 7(a). The cross-sectional microstructures during and after the FIB process are shown in Fig. 7(c–d), respectively. Few microscopic cracks are detected in Fig. 7(c), as indicated by the arrows. The overall cross-section TEM micrographs are further shown in Fig. 7(e); the enlarged views with different features are shown in Fig. 7(f–g). The yellow ellipse indicated by the arrow is the position marker. The thickness of the worn subsurface is ~10 μm. Fig. 8 further shows the detailed STEM-EDS mapping of the cracking region. Fig. 8(a) is the HAADF micrograph of the substructure. Fig. 8(b–g) is the EDS mapping of the selected dashed area to depict the distribution of the chemical compositions of Cu, O, Pt, Ni, Fe, and Sn, respectively. This confirms the existence of the Cu_2O layer and the Cu_2O and NG Cu layer. Moreover, the dotted lines show the track of the crack propagation, indicating that the wear-induced cracks initiate from the Cu_2O layer and then propagate along the Cu_2O/nanocomposite boundaries. The subsurface structure under the worn surface comprises typical gradient nanostructures and several layers, from top to bottom: top ~500 nm Cu_2O, ~500 nm nanocomposite layer, ~500 nm NG Cu, ~500 nm NG + UFG Cu, ~1 μm UFG Cu, ~2 μm FG Cu, and the left deformed CG Cu. The atomic-scale observations, including the diffraction analyses, HRTEM, and STEM–EDS characterizations were conducted in representative regions.

3.3.3. *Atomic-scale observation*

Representative TEM and HRTEM micrographs of the top worn surface of the nanocomposite layer are shown in Fig. 9. Fig. 9(a) is the TEM micrograph of the top layer (beneath the Pt layer), with the inset showing the SAED pattern of the Cu_2O diffraction rings, e.g., $d_{\{110\}Cu_2O}$ = 3.0 Å. The applied lattice parameters for crystalline Cu_2O are $a = b =$

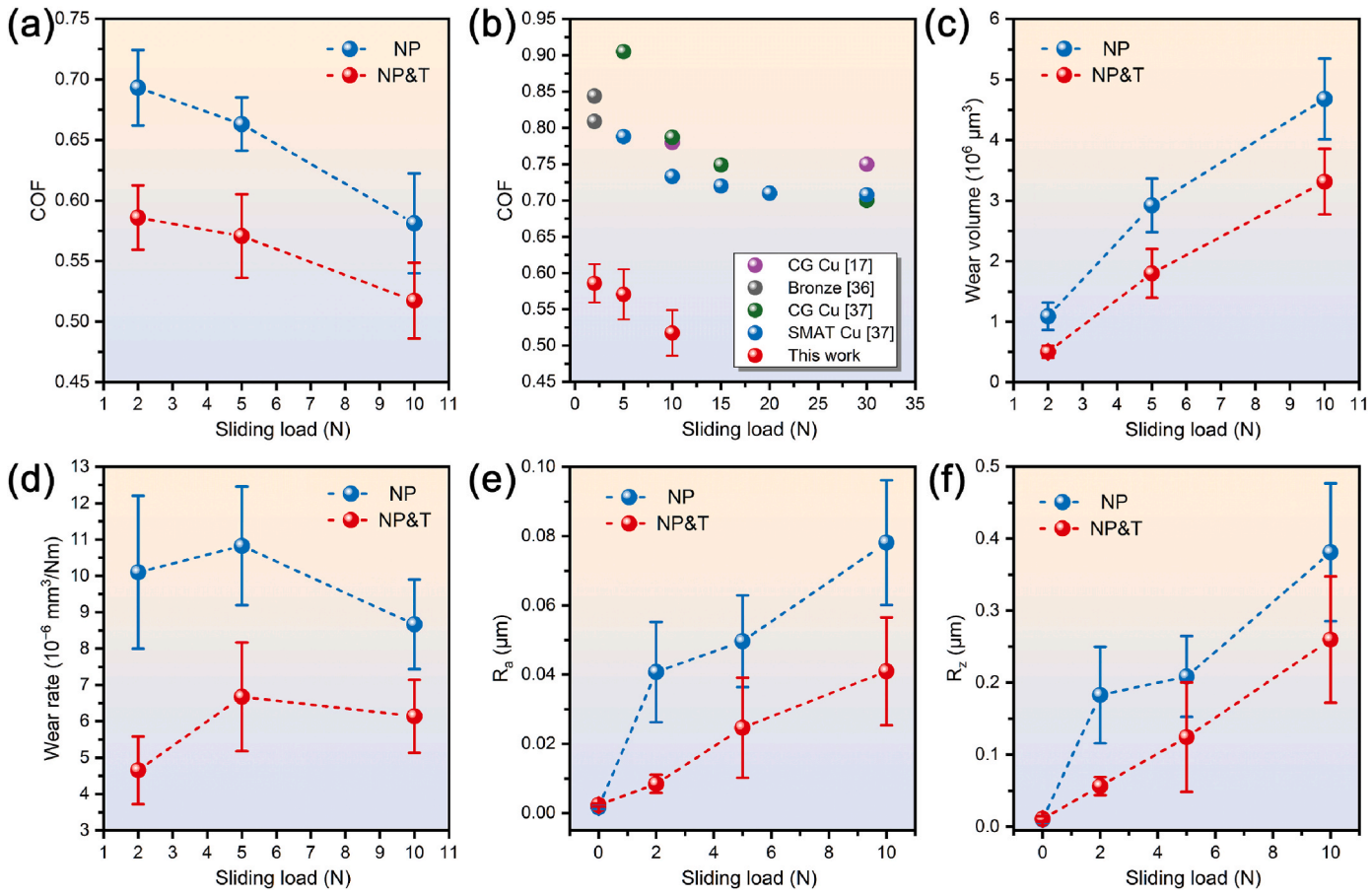

Fig. 5. (a) Variations of the steady-state COFs with the loads. (b) Comparison of COFs of NP&T sample under different loads investigated in this work and those reported in previous studies [17,36,37]. Variations of (c) wear volumes, (d) wear rates, (e) R_a, and (f) R_z with sliding loads for NP and NP&T samples.

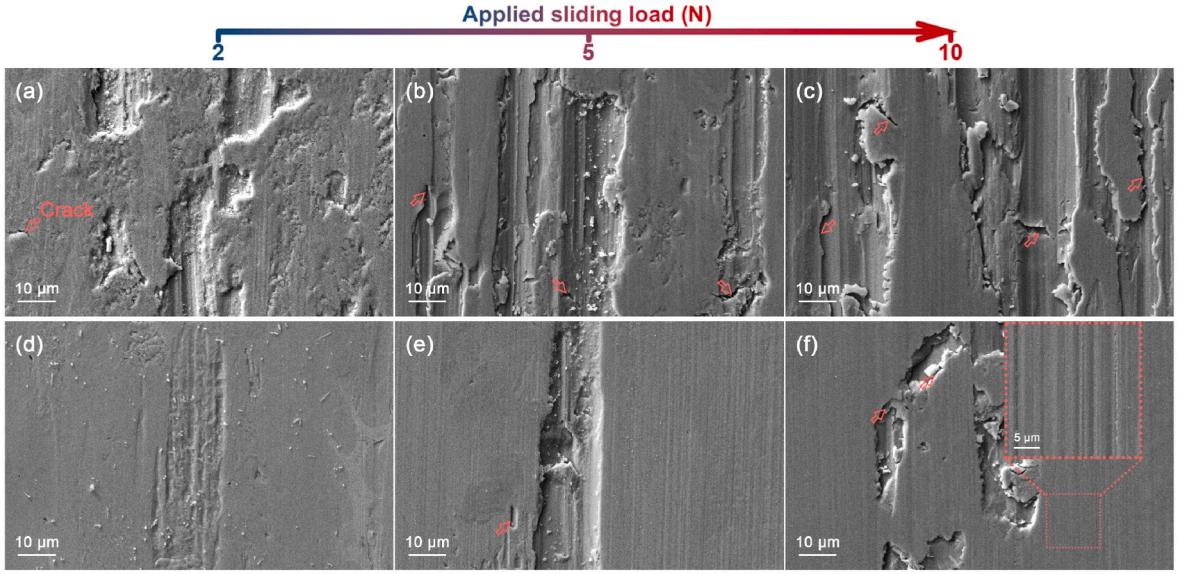

Fig. 6. Respective SEM micrographs of the worn surfaces of (a–c) NP and (d–f) NP&T specimens under various loads of (a, d) 2 N, (b, e) 5 N, and (c, f) 10 N. The arrows indicate the cracks at the worn surface. Inset in (f) shows the detail of the smooth plastic zone in NP&T sample under sliding load of 10 N.

$c = 4.27$ Å, and $\alpha = \beta = \gamma = 90°$ in this study [34,38]. The white area in Fig. 9(a) is the cavity between the Pt layer and Cu_2O layer. Fig. 9(b) shows the enlarged TEM view of the cracking region at the worn surface. This wear-induced crack is indicated by the arrow in Fig. 7(b). Fig. 9(c) depicts the substructure of the Cu_2O + NG Cu nanocomposite. A magnified view of the nanocomposite is presented in Fig. 9(d), with the inset showing the SAED patterns of the Cu_2O + NG Cu area. The Cu nanograins, marked with arrows, have an average diameter of ~20 nm.

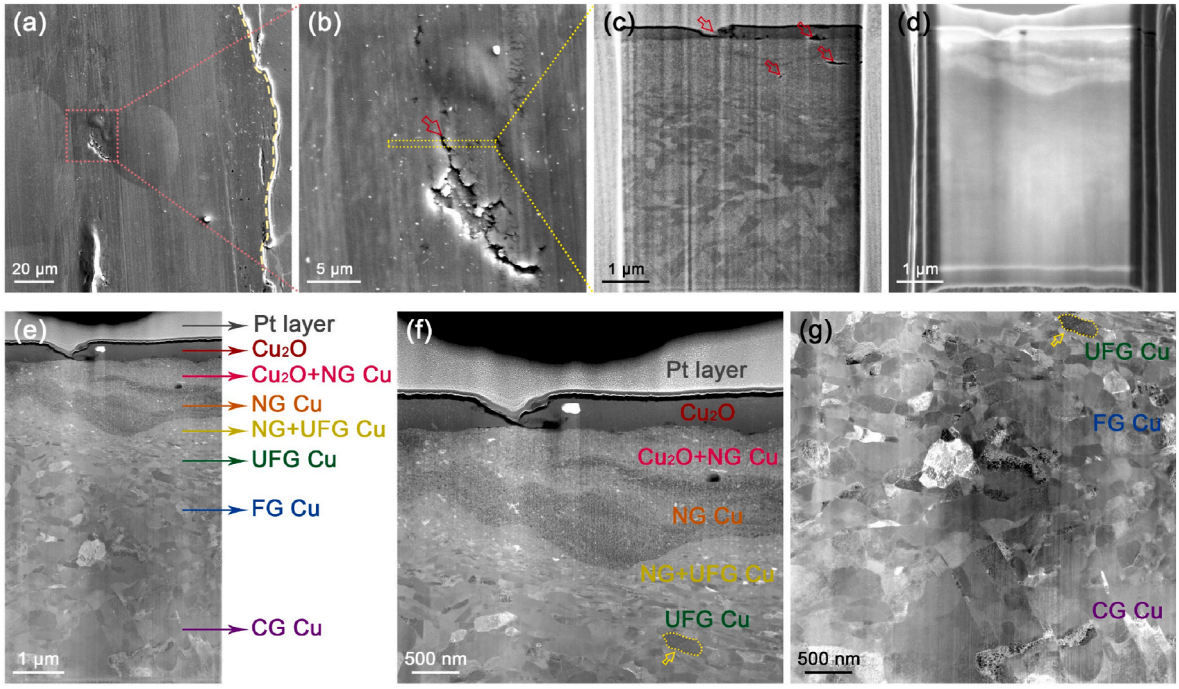

Fig. 7. Cross-sectional SEM and TEM characterizations of the worn surface in NP&T alloy after sliding under 10 N. (a) SEM micrograph of the worn subsurface. (b) An enlarged view of the dotted region in (a); the lift-out FIB technique was conducted at the rectangle area with a sliding-induced crack. (c) SEM image showing the cross-sectional microstructure during the FIB milling process; the underlying micro cracks are indicated by the arrows. (d) SEM image after the FIB milling process, showing the lamellar structure. (e) Cross-section TEM image with marked characteristic lamellar regions. (f–g) Enlarged TEM views of the friction-induced microstructures.

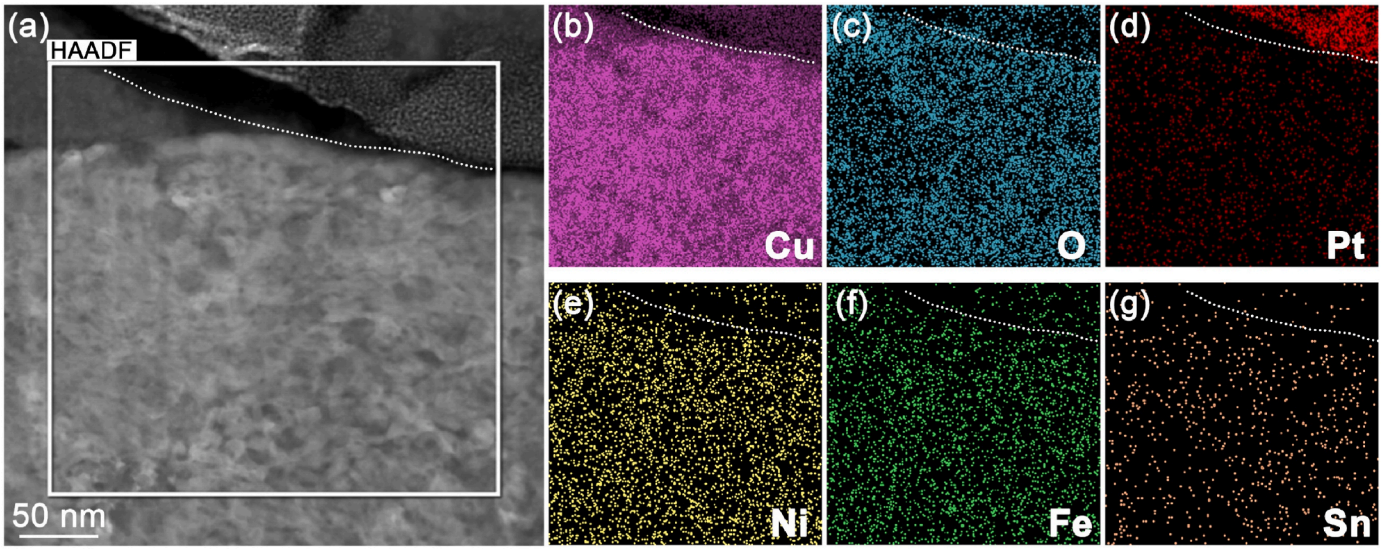

Fig. 8. The STEM-EDS mapping of the cracking region in worn NP&T specimen: (a) the HAADF micrograph, EDS mapping of the selected region in (a) indicating the chemical compositions of (b) Cu, (c) O, (d) Pt, (e) Ni, (f) Fe, and (g) Sn. The dotted lines indicate the track of the crack propagation.

Moreover, Fig. 9(e) shows the HRTEM of the boundary between the Cu_2O layer and the nanocomposite layer, with the inverse fast Fourier transform (IFFT) of the dotted-contoured region in Fig. 9(f). Notably, the average interplanar spacings of $(111)_{Cu_2O}$ and $(111)_{fcc\ Cu}$ are measured to be $d_{(111)Cu_2O} = 2.5$ Å and $d_{(111)fcc\ Cu} = 2.1$ Å, respectively. Fig. 9(g–h) also show another set of Fourier transform (FFT) and IFFT images of the Cu_2O + NG Cu concomitant scenario. Cu_2O and fcc Cu are identified, respectively, with white and violet arrows in the FFT spots. The above analyses suggest that the wear-affected area of the NP&T alloy consists the Cu_2O and equiaxed nanocomposite layers on the topmost surface of the gradient severe plastic deformation region.

As regards the NG Cu layer underneath the nanocomposite layer, Fig. 10(a) shows the TEM micrograph of the NG Cu decorated with the nano twins (marked by the blue arrows). Fig. 10(b) presents the magnified TEM image to depict the distribution of nano twins inside the NG Cu. Fig. 10(c) further shows a typical HRTEM image of one twinned NG Cu, with the grain boundary delineated by the violet dotted line. Fig. 10(d) is the enlarged atom resolved IFFT of the region outlined by the white square in Fig. 10(c). The inset shows the FFT patterns and the atomic arrangements of the matrix (marked by "M") and twin (marked

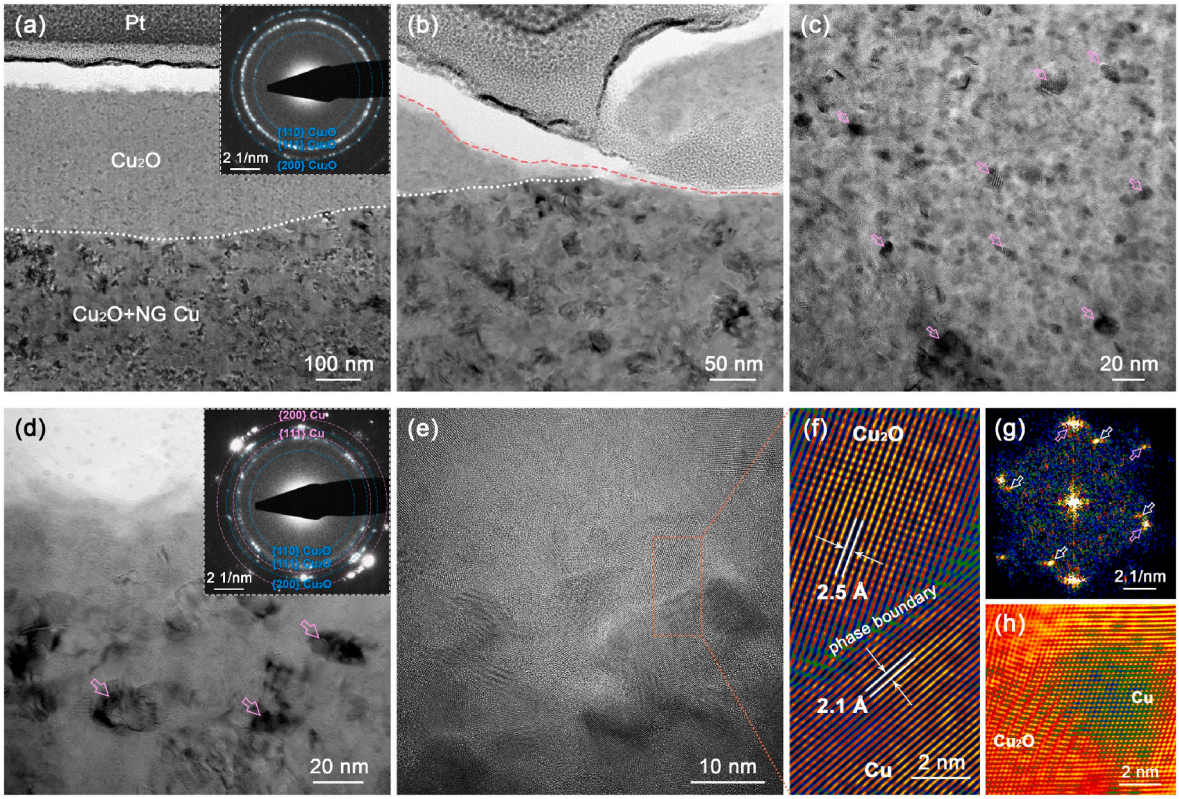

Fig. 9. Representative TEM and HRTEM micrographs of the nanocomposite layer approaching the worn surface. (a) TEM image of the top layer, with the inset showing the SAED pattern of the Cu_2O area. (b) Enlarged TEM view of the cracking region at the worn surface. (c) TEM image depicting the structure of the nanocomposite with Cu_2O + NG Cu. (d) Magnified view of the nanocomposite layer, with the inset showing the SAED patterns of the Cu_2O + NG Cu area. (e) HRTEM image showing the boundary between the Cu_2O layer and the nanocomposite layer. (f) IFFT of the dotted region in (e). (g) FFT and (h) IFFT maps of the Cu_2O + NG Cu concomitant scenario.

by "T"). Moreover, numerous stacking faults (SFs) are also observed in the fcc NG Cu matrix, as marked by the arrows in Fig. 10(e). Fig. 10(f) is the corresponding IFFT of the dotted-contour region in (e), with the inset showing the FFT map of the matrix and SFs. Intriguingly, high-density deformation nano twins and SFs originate from one side of the grain boundary and penetrate the interior on the opposite side. An NG Cu layer decorated with these nanotwins and SFs would display a high strength and superior ductility [39,40], thus improving the tribological properties of the NP&T alloy. The nano twins and SFs structures with excellent deformability could provide the plasticity to accommodate the strain/stress imposed from the sliding process. The cooperative effect of high-density deformation nano twins and SFs could be realized to effectively accommodate the plastic deformation and suppress the surface roughening and delaminating for the enhanced tribological performance [41].

Representative TEM images of the microstructural evolution at various depths below the worn surface of the NP&T alloy are shown in Fig. 11. The deformed microstructural scenarios with layers NG + UFG Cu, UFG Cu, FG Cu, and CG Cu are depicted in Fig. 11(a–d), respectively. The blue arrows show the distribution of deformed grains with nano twins. Specifically, the inset of Fig. 11(d) presents the SAED map of the triplex microstructure of the matrix, hierarchical nano twins (blue and red arrows), and precipitates (yellow arrows). This indicates that the plastic deformation mode of the gradient layers below the nanocomposite layer (Fig. 9) is twinning mediated deformation.

3.4. Wear mechanisms of the homogeneous and gradient Cu alloys

For the homogeneous precipitates-strengthening Cu alloy, NP sample possesses a decent COF (e.g., 0.58 at 10 N), compared with the traditional CG Cu and bronze (Fig. 5(a-b)). The precipitates-strengthening alloys usually possess higher hardness than the CG alloy due to the precipitation hardening effect, thus being beneficial for the friction and wear resistance according to the Archard equation [11,12]. The brittle tribo-layers in NP sample are inclined to generate and delaminate to form the deep scars and cracks (Fig. 6) due to the sliding-induced strain localization [15], which could be inferred as the abrasive wear mechanism.

After SMAT process, the gradient nanostructure was generated in the NP&T alloy (Figs. 1 and 2). Besides, gradient nanograins and gradient nanotwins could be stimulated with the misfit dislocations in the fcc-Cu/bcc-Fe semi-coherent interfaces [5]. Furthermore, the inherent gradient structures in the NP&T alloy could achieve strain delocalization with superior stability under repeated sliding loads, thus suppressing surface deformation and improving the friction and wear resistance [15,17,18,37]. Thus, the strategy of GNS in precipitates-strengthening copper alloy via SMAT could reduce COF and enhance the wear resistance to elevate the tribological performance.

3.5. Effect of the gradient nanostructure on wear-resistant performance

The above results and analyses demonstrate the superior tribological properties of the SMAT-processed GNS NP&T alloy, as expressed by the COFs, wear volumes, wear rates, and worn surface roughness, compared with the original NP alloy. The wear-induced substructure in NP&T alloy is comprised of the twinning and SFs mediated gradient layers (i.e., deformed CG Cu, FG Cu, UFG Cu, NG + UFG Cu, and NG Cu layer) and nanocomposite layers from bottom to the topmost surface. The depth-dependent gradient nanostructure newly formed during the friction process would realize strain delocalization, thereby yielding novel

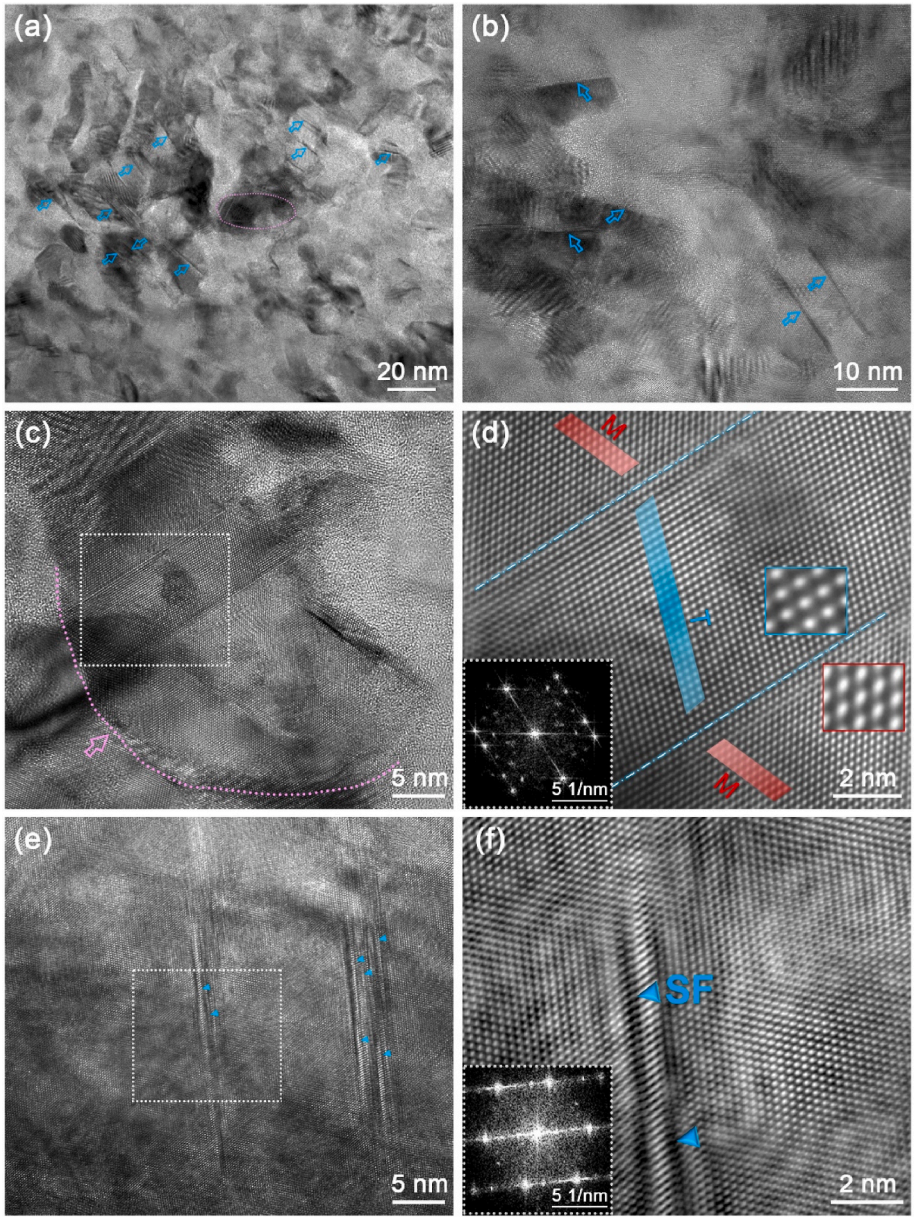

Fig. 10. (a) TEM micrograph of the NG Cu layer underneath the nanocomposite layer, decorated with the nano twins indicated by the blue arrows. (b) Magnified TEM micrograph indicating the distribution of nano twins. (c) HRTEM image of one typical nano grain. (d) Atom-resolved IFFT of the dotted region in (c), with the inset showing the FFT map and the atomic arrangements of the matrix and twin. (e) HRTEM image presenting the nano grain embedded with SFs. (f) IFFT of the dotted region in (e), with the inset showing the FFT map of the matrix and SFs.

tribological performance characteristics. The regenerative COFs are presented in Fig. 12 as functions of the sliding time for the NP and NP&T alloys under a 2 N sliding load over an extended time of 18000 s (5 h) after sliding for 1800 s. After sliding for ~2 h, a greater difference emerges between the COFs for the NP and NP&T samples. This result indicates that the sliding-induced NP&T alloy exhibits a better tribological performance due to the wear-induced in situ gradient substructure. The concept of the gradient nanostructure is beneficial for designing the wear-resistant alloys [31,32,41]. The wear-induced substructure in NP&T alloy is comprised of the twinning and SFs mediated gradient layers (i.e., deformed CG Cu, FG Cu, UFG Cu, NG + UFG Cu, and NG Cu layer) and nanocomposite layers, leading to the novel tribological performance. The strategy of the inherent and newly formed gradient nanostructures is beneficial in designing the high-performance copper alloys.

4. Conclusions

In summary, we have investigated the relationship between the gradient microstructures after SMAT process and the corresponding tribological properties of the nanoprecipitates strengthened copper alloy. Moreover, the macro-, micro-, and atomic-scale friction and wear mechanisms and its effect on the wear-resistant performance were further determined. The main conclusions are summarized in the following.

(1) After the SMAT process, the NP&T alloy exhibits the typical gradient microstructure, including the distribution of grains and dislocation densities.
(2) The friction and wear tests under various loads were conducted and analyzed to evaluate the tribological properties of the studied copper alloys. The NP&T alloy possessed distinctly lower COFs

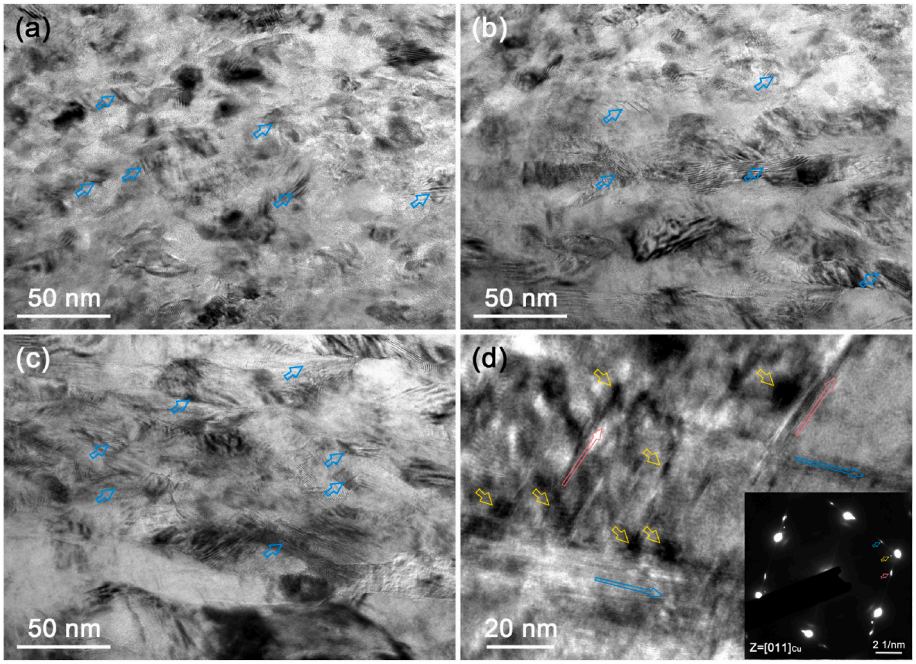

Fig. 11. Representative TEM images presenting the microstructure evolution at various depth below the worn surface of NP&T alloy: (a) NG + UFG Cu, (b) UFG Cu, (c) FG Cu, (d) deformed CG Cu area, with the inset showing the SAED map of the matrix, hierarchical nano twins, and precipitates (marked by the yellow arrows). The blue arrows show the distribution of nano-twin decorated grains.

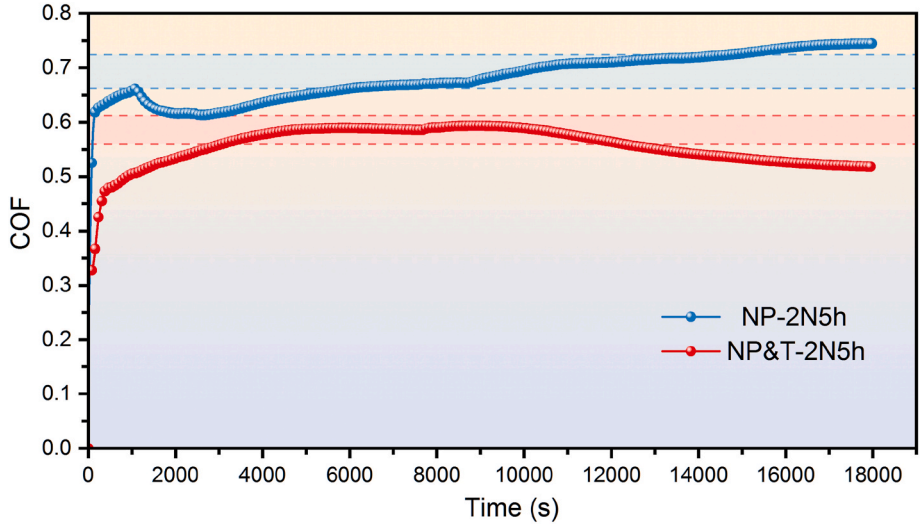

Fig. 12. COFs versus sliding time for NP and NP&T alloys under the sliding load of 2 N for 18000 s (5 h) after sliding for 1800 s.

than those similar copper alloys. Simultaneously, the NP&T invariably exhibits much reduced wear volumes, wear rates, and worn surface roughness compared to the NP counterpart, indicating the superior tribological properties in NP&T alloy.

(3) For the homogeneous NP alloy, the tribo-layers are inclined to generate and delaminate to form the deep scars and cracks ascribed to the sliding-induced strain localization. However, the inherent gradient structures in NP&T alloy could achieve strain delocalization, thus suppressing surface deformation and improving the wear resistance.

(4) The wear-induced substructure in NP&T alloy is comprised of the twinning and SFs mediated gradient layers (i.e., deformed CG Cu, FG Cu, UFG Cu, NG + UFG Cu, and NG Cu layer) and nanocomposite layers, leading to the novel tribological performance.

Declaration of competing interest

The authors declare that they have no known competing financial interests or personal relationships that could have appeared to influence the work reported in this paper.

Acknowledgments

The authors acknowledge the financial support received from the National Natural Science Foundation of China (Nos. 52201060 and U21A2044), China Postdoctoral Science Foundation (Nos. BX20220035 and 2022M710347), Science Center for Gas Turbine Project (No. P2022-B-IV-008-001), and PolyU grant (Nos. 1-BBR1 and G-YWAA).

References

[1] Li X, Lu L, Li J, Zhang X, Gao H. Mechanical properties and deformation mechanisms of gradient nanostructured metals and alloys. Nat Rev Mater 2020;5(9):706–23. https://doi.org/10.1038/s41578-020-0212-2.

[2] Sun LG, Wu G, Wang Q, Lu J. Nanostructural metallic materials: structures and mechanical properties. Mater Today 2020;38:114–35. https://doi.org/10.1016/j.mattod.2020.04.005.

[3] Li X, Lu K. Playing with defects in metals. Nat Mater 2017;16(7):700–1. https://doi.org/10.1038/nmat4929.

[4] Shi R, Ma Y, Wang Z, Gao L, Yang X-S, Qiao L, Pang X. Atomic-scale investigation of deep hydrogen trapping in NbC/α-Fe semi-coherent interfaces. Acta Mater 2020;200:686–98. https://doi.org/10.1016/j.actamat.2020.09.031.

[5] Shi R, Fu H, Chen K, Sun W, Wang Z, Qiao L, Yang X-S, Pang X. Combining synergetic effects of gradient nanotwins and nanoprecipitates in heterogeneous bronze alloy. Acta Mater 2022;229. https://doi.org/10.1016/j.actamat.2022.117831.

[6] Craddock PT. Three thousand years of copper alloys: from the bronze age to the industrial revolution. In: England PA, Van Zelst L, editors. Application of science in examination of works of art. Proceedings of the seminar. Boston: Museum of Fine Arts; 1985. p. 59–67.

[7] Glaeser WA. Wear properties of heavy loaded copper-base bearing alloys. J Occup Med 1983;35(10):50–5. https://doi.org/10.1007/bf03338390.

[8] Fontanari V, Benedetti M, Straffelini G, Girardi C, Giordanino L. Tribological behavior of the bronze–steel pair for worm gearing. Wear 2013;302(1–2):1520–7. https://doi.org/10.1016/j.wear.2013.01.058.

[9] Ajayi OO, Lorenzo-Martin C. Enhancement of bronze alloy surface properties by FSP second-phase particle incorporation. Wear 2017;376–377:1055–63. https://doi.org/10.1016/j.wear.2017.01.059.

[10] Chen K, Zhang J, Chen X, Wang Z, Shi R, Zhang A. The effect of iron on the microstructure and mechanical properties of a cast Cu–12Sn-1.5Ni (wt. %) alloy. Mater Sci Eng, A 2020;785:139330. https://doi.org/10.1016/j.msea.2020.139330.

[11] Archard JF. Contact and rubbing of flat surfaces. J Appl Phys 1953;24(8):981–8. https://doi.org/10.1063/1.1721448.

[12] Rupert TJ, Schuh CA. Sliding wear of nanocrystalline Ni–W: structural evolution and the apparent breakdown of Archard scaling. Acta Mater 2010;58(12):4137–48. https://doi.org/10.1016/j.actamat.2010.04.005.

[13] Hall EO. The deformation and ageing of mild steel: III discussion of results. Proc Phys Soc Lond B 1951;64(9):747. https://doi.org/10.1088/0370-1301/64/6/305.

[14] Petch NJ. The ductile-brittle transition in the fracture of α-iron: I. Philos Mag A 1958;3(34):1089–97. https://doi.org/10.1080/14786435808237038.

[15] Chen X, Han Z, Li X, Lu K. Lowering coefficient of friction in Cu alloys with stable gradient nanostructures. Sci Adv 2016;2(12):e1601942. https://doi.org/10.1126/sciadv.1601942.

[16] Prasad SV, Battaile CC, Kotula PG. Friction transitions in nanocrystalline nickel. Scripta Mater 2011;64(8):729–32. https://doi.org/10.1016/j.scriptamat.2010.12.027.

[17] Chen X, Han Z, Lu K. Friction and wear reduction in copper with a gradient nano-grained surface layer. ACS Appl Mater Interfaces 2018;10(16):13829–38. https://doi.org/10.1021/acsami.8b01205.

[18] Chen X, Han Z, Li XY, Lu K. Friction of stable gradient nano-grained metals. Scripta Mater 2020;185:82–7. https://doi.org/10.1016/j.scriptamat.2020.04.041.

[19] Cheng Z, Zhou H, Lu Q, Gao H, Lu L. Extra strengthening and work hardening in gradient nanotwinned metals. Science 2018;362(6414):eaau1925. https://doi.org/10.1126/science.aau1925.

[20] Wei Y, Li Y, Zhu L, Liu Y, Lei X, Wang G, Wu Y, Mi Z, Liu J, Wang H, Gao H. Evading the strength-ductility trade-off dilemma in steel through gradient hierarchical nanotwins. Nat Commun 2014;5:3580. https://doi.org/10.1038/ncomms4580.

[21] Lu K. Stabilizing nanostructures in metals using grain and twin boundary architectures. Nat Rev Mater 2016;1(5):1–13. https://doi.org/10.1038/natrevmats.2016.19.

[22] Olugbade TO, Lu J. Literature review on the mechanical properties of materials after surface mechanical attrition treatment (SMAT). Nano Mater. Sci. 2020;2(1):3–31. https://doi.org/10.1016/j.nanoms.2020.04.002.

[23] Lu K, Lu J. Nanostructured surface layer on metallic materials induced by surface mechanical attrition treatment. Mater Sci Eng, A 2004;375–377:38–45. https://doi.org/10.1016/j.msea.2003.10.261.

[24] Fang TH, Li WL, Tao NR, Lu K. Revealing extraordinary intrinsic tensile plasticity in gradient nano-grained copper. Science 2011;331(6024):1587–90. https://doi.org/10.1126/science.1200177.

[25] Liu XC, Zhang HW, Lu K. Formation of nano-laminated structure in nickel by means of surface mechanical grinding treatment. Acta Mater 2015;96:24–36. https://doi.org/10.1016/j.actamat.2015.06.014.

[26] Wang JJ, Tao NR, Lu K. Revealing the deformation mechanisms of nanograins in gradient nanostructured Cu and CuAl alloys under tension. Acta Mater 2019;180:231–42. https://doi.org/10.1016/j.actamat.2019.09.021.

[27] Zhang YZ, Wang JJ, Tao NR. Tensile ductility and deformation mechanisms of a nanotwinned 316L austenitic stainless steel. J Mater Sci Technol 2020;36:65–9. https://doi.org/10.1016/j.jmst.2019.02.008.

[28] Yuan S, Gan B, Qian L, Wu B, Fu H, Wu H-H, Cheung CF, Yang X-S. Gradient nanotwinned CrCoNi medium-entropy alloy with strength-ductility synergy. Scripta Mater 2021;203:114117. https://doi.org/10.1016/j.scriptamat.2021.114117.

[29] Fu H, Zhou X, Wu B, Qian L, Yang X-S. Atomic-scale dissecting the formation mechanism of gradient nanostructured layer on Mg alloy processed by a novel high-speed machining technique. J Mater Sci Technol 2021;82:227–38. https://doi.org/10.1016/j.jmst.2020.10.086.

[30] Wu B, Fu H, Zhou X, Qian L, Luo J, Zhu J, Lee WB, Yang X-S. Severe plastic deformation-produced gradient nanostructured copper with a strengthening-softening transition. Mater Sci Eng, A 2021;819:141495. https://doi.org/10.1016/j.msea.2021.141495.

[31] Luo J, Sun W, Liang D, Chan KC, Yang X-S, Ren F. Superior wear resistance in a TaMoNb compositionally complex alloy film via in-situ formation of the amorphous-crystalline nanocomposite layer and gradient nanostructure. Acta Mater 2023;243:118503. https://doi.org/10.1016/j.actamat.2022.118503.

[32] Liu C, Li Z, Lu W, Bao Y, Xia W, Wu X, Zhao H, Gault B, Liu C, Herbig M, Fischer A, Dehm G, Wu G, Raabe D. Reactive wear protection through strong and deformable oxide nanocomposite surfaces. Nat Commun 2021;12(1):5518. https://doi.org/10.1038/s41467-021-25778-y.

[33] Zhu W, Zhao C, Zhang Y, Kwok CT, Luan J, Jiao Z, Ren F. Achieving exceptional wear resistance in a compositionally complex alloy via tuning the interfacial structure and chemistry. Acta Mater 2020;188:697–710. https://doi.org/10.1016/j.actamat.2020.02.039.

[34] Chen X, Ma Y, Yang Y, Meng A, Han ZX, Han Z, Zhao YH. Revealing tribo–oxidation mechanisms of the copper–WC system under high tribological loading. Scripta Mater 2021;204. https://doi.org/10.1016/j.scriptamat.2021.114142.

[35] Bharatish A, Harish V, Bathe RN, Senthilselvan J, Soundarapandian S. Effect of scanning speed and tin content on the tribological behavior of femtosecond laser textured tin-bronze alloy. Opt Laser Technol 2018;108:17–25. https://doi.org/10.1016/j.optlastec.2018.06.041.

[36] Tavakoli A, Liu R, Wu XJ. Improved mechanical and tribological properties of tin–bronze journal bearing materials with newly developed tribaloy alloy additive. Mater Sci Eng, A 2008;489(1–2):389–402. https://doi.org/10.1016/j.msea.2007.12.030.

[37] Zhang YS, Han Z, Wang K, Lu K. Friction and wear behaviors of nanocrystalline surface layer of pure copper. Wear 2006;260(9–10):942–8. https://doi.org/10.1016/j.wear.2005.06.010.

[38] Mallik M, Monia S, Gupta M, Ghosh A, Toppo MP, Roy H. Synthesis and characterization of Cu_2O nanoparticles. J Alloys Compd 2020;829. https://doi.org/10.1016/j.jallcom.2020.154623.

[39] Lu Q, You Z, Huang X, Hansen N, Lu L. Dependence of dislocation structure on orientation and slip systems in highly oriented nanotwinned Cu. Acta Mater 2017;127:85–97. https://doi.org/10.1016/j.actamat.2017.01.016.

[40] Zhu YT, Liao XZ, Wu XL. Deformation twinning in nanocrystalline materials. Prog Mater Sci 2012;57(1):1–62. https://doi.org/10.1016/j.pmatsci.2011.05.001.

[41] Wu B, Fu H, Sun WT, Yang WQ, Luo JS, Yang XS. Significantly lowered coefficient of friction in copper alloy with a gradient nanograined-nanotwinned surface layer. Wear 2022;510–511:204517. https://doi.org/10.1016/j.wear.2022.204517.